

Department of Engineering Physics and Mathematics  
Helsinki University of Technology  
FIN-02015 HUT, Finland

**Investigations of Solid-Liquid Interfaces  
in Helium at Ultralow Temperatures**

**Viktor Tsepelin**

Low Temperature Laboratory

Dissertation for the Degree of Doctor of Science in Technology to be presented with due permission of the Department of Engineering Physics and Mathematics for public examination and debate in Auditorium F1 at the Helsinki University of Technology (Espoo, Finland) on the 7th of June, at 12 o'clock noon.

Espoo 2001

**Keywords:** Interfacial phenomena, solid-liquid interface, helium crystals, morphology, roughening transitions, growth anisotropy, multiple-beam interferometry, phase-shift technique.

## Abstract

This Thesis describes ultralow temperature studies of helium quantum crystals. Owing to the surrounding superfluid, small latent heat of crystallization and correspondingly short relaxation times, which are unreachable in ordinary crystals, helium crystals offer a unique and clean modeling system to study surface phenomena in a solid. The measurements of the crystal shape and growth rates are essential in providing the microscopic understanding of crystal growth.

Optical observations are probably the most direct way to quantify the surface of crystals. The results presented in this Thesis were obtained with the help of two very powerful experimental techniques that were successfully adopted for ultralow temperature applications: optical interferometry and high-precision pressure measurements.

The optical investigations on  $^3\text{He}$  crystals revealed altogether eleven types of facets at temperatures well below 1 mK, while previously only three facet types have been seen. The growth rates of rough and smooth surface states were explored and show significant anisotropy. The measured growth velocities of different facet types indicate that the main growth mechanism is spiral growth in the regime of suppressed mobility. Important thermodynamic parameters of an interface such as the width of an elementary step and the step free energy were directly deduced from the observed growth kinetics. Results suggest that coupling of the interface to the underlying crystal lattice is relatively “strong” in  $^3\text{He}$  crystals.

Measurements of the spiral growth of the **c**-facet on  $^4\text{He}$  crystals in the presence of a small number of  $^3\text{He}$  atoms were also conducted. They show suppression of the crystal growth velocity with the increase of the  $^3\text{He}$  atom concentration and indicate “weak” coupling of the interface to the crystal lattice in  $^4\text{He}$ .

# Contents

<b>1</b>	<b>Introduction</b>	<b>1</b>
1.1	$^4\text{He}$ crystals . . . . .	3
1.2	$^3\text{He}$ crystals . . . . .	5
<b>2</b>	<b>Experimental apparatus</b>	<b>8</b>
2.1	Ultralow temperature probe for optical measurements on $^3\text{He}$ crystals . . . . .	8
2.2	Setup for c-facet studies on $^4\text{He}$ crystals . . . . .	11
<b>3</b>	<b>Experiments on solid-liquid interface of <math>^3\text{He}</math></b>	<b>14</b>
3.1	Nucleation of crystals . . . . .	14
3.2	Morphological studies . . . . .	16
3.3	Anisotropy of growth kinetics . . . . .	18
<b>4</b>	<b>Growth kinetics of c-facets of <math>^4\text{He}</math> crystals</b>	<b>24</b>
<b>5</b>	<b>Discussion</b>	<b>27</b>
<b>6</b>	<b>Publications</b>	<b>29</b>
<b>7</b>	<b>The author's contribution</b>	<b>31</b>
	<b>Acknowledgements</b>	<b>32</b>
	<b>References</b>	<b>33</b>



# 1 Introduction

The recent development of low-temperature technologies has shed light on many physical phenomena previously hidden by Nature. Perhaps the most fascinating secrets revealed until now are the superconductivity of metals and the superfluidity of the helium liquids. Not quite as widely known, but definitely also very exciting, are the properties exhibited by the quantum crystals of helium.

Helium crystals are truly exceptional. The crystalline phase can stay in equilibrium with the liquid down to zero temperature because of the quantum fluctuations which dominate over the weak van der Waals interaction of the atoms. To solidify helium, a moderate external pressure has to be applied even at  $T = 0$  K. Depending on pressure and temperature, solid helium exhibits *hcp*, *bcc* or *fcc* crystal structures. At low enough temperatures, the melting curve is nearly horizontal so the latent heat becomes very small. At the same time, the highly mobile superfluid phase makes the crystal growth and equilibrium practically independent of heat and mass flow considerations.

Owing to the quantum nature of the helium crystals, point surface defects such as elementary kinks on an atomic step can be regarded as quasiparticles, which move along the step as free particles. Motion of the crystal surface is therefore only hampered by interactions with elementary excitations in the bulk phases. Thus the morphological changes in helium crystals can take place very rapidly on a time scale of a fraction of a second. Among other properties worth noting is the ultimate purity of the sample, since all other substances are frozen out. To complete the picture, it should be pointed out that helium has two stable isotopes,  $^4\text{He}$  and  $^3\text{He}$ . They differ substantially from each other, since a  $^4\text{He}$  atom is a boson while  $^3\text{He}$  is a fermion. The short shape relaxation time of helium crystals has enabled systematic experimental and theoretical studies of both their equilibrium and kinetic properties. In summary, helium crystals thus offer a unique and clean modeling system to study surface phenomena in solids.

Generally, the crystalline boundary can exist in two different states: rounded (atomically rough) or faceted (atomically smooth). Let us imagine a step on an otherwise flat surface, with the left part one atomic layer higher than the right one. The step has a finite width which is determined by the coupling strength of the interface to the crystal lattice. If the coupling is strong the step is sharp, while in the case of weak coupling it is blurred over some distance  $\xi$ , see Fig. 1. The number of thermally nucleated steps on the crystal surface increases with temperature and when the distance between the steps and their width become comparable, the surface becomes rough. The phase transition between

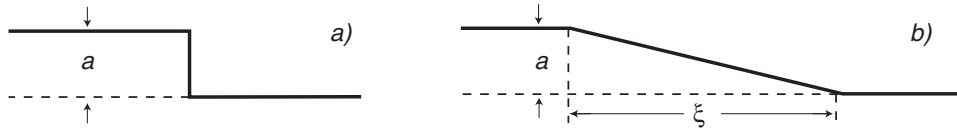


Figure 1: Profile of an elementary step: *a*) strong- and *b*) weak-coupling limit.

the rough and faceted surface states is called the roughening transition. It is generally believed that the roughening transition belongs to the Kosterlitz-Thouless universality class [1,2].

According to many theoretical models, crystal shapes are believed to be entirely faceted at zero temperature [3], although there has been some controversy on this point when zero-point fluctuations are large [1,4]. The surface of quantum crystals has been predicted to be in a quantum-rough state even at absolute zero due to the delocalization of steps and kinks [4]. On the other hand, it has been shown that this is unlikely to happen [1]. The experiments conducted show arguments in favor of both theories, for reviews see Refs. [5,6] and references therein.

Important thermodynamic parameters of an interface can be directly deduced from the equilibrium crystal profile and its growth kinetics. Measurements of macroscopic quantities, such as the size of a facet, the growth rate and the roughening transition temperature can reveal microscopic parameters, such as the free energy of the step, and the coupling of the interface to the crystal lattice.

Optical observations are probably the most direct way to quantify the surface of crystals. However, all practical technicalities such as the imaging optical scheme, data collection procedure, etc., may vary for different experimental conditions and according to the goals that one is trying to achieve.

Most of the solid-helium related studies have so far been carried out using a conventional optical cryostat with several sets of windows and with most of the optical components located at room temperature [7–9]. Accessing temperatures lower than 20 mK in such a configuration is an extremely difficult task; the thermal radiation through the optical windows limits the lowest achievable temperature of the measurements. Recently, optical studies conducted at much lower temperatures have become possible after a new type of technical approach has been put forward by two groups of investigators [10–12]. Both groups had their optical instruments, including a high-resolution imaging system, confined inside the 4-K vacuum jacket of their experimental apparatus. Owing to this

technical improvement, the external heat loads caused by the presence of the “hot” optical windows can be avoided, or at least greatly reduced.

The results presented in this Thesis were obtained with the help of two very powerful experimental techniques that we have successfully adopted for ultralow temperature applications: optical interferometry and high-precision pressure measurements. Morphology and growth kinetics of *bcc*- $^3\text{He}$  crystals were the major subject of these studies during the past four years. To achieve temperatures well below 1 mK, the cryogenic part of the low-temperature probe was considerably improved as compared with the one used before [13]. A low-temperature multiple-beam interferometer was developed and built for these studies. Publications [P1, P2] report on the first successful attempts to nucleate and study  $^3\text{He}$  crystals below 1 mK using this new interferometric setup. Measurements on the crystal morphology conducted with the help of the phase-shift technique are described in detail in publication [P3]. The studies of growing  $^3\text{He}$  crystals revealed a number of new types of facets never seen before [P4—P6]. The growth rates of the rough and faceted surfaces were measured at 0.55 mK. The results suggest that the step-step interactions are of elastic origin [P5]. The step energies for most of these newly observed facets were calculated in the same publication. Finally, the width of an elementary step on the **c**-facet of  $^4\text{He}$  crystals was probed by scattering of  $^3\text{He}$  atoms, as described in publication [P7].

## 1.1 $^4\text{He}$ crystals

$^4\text{He}$  is the more common of the two stable isotopes of helium. It is used, as we all know, to inflate balloons. In some wells, natural gas can contain as much as 10% of  $^4\text{He}$ . The liquid-solid phase diagram of  $^4\text{He}$  as a function of pressure and temperature is shown in Fig. 2. Helium gas liquefies at a temperature of 4.2 K ( $p = 1$  bar) and remains liquid down to zero temperature. Liquid  $^4\text{He}$  becomes superfluid at  $T_\lambda = 2.17$  K, where it has effectively zero viscosity and can flow through “superleaks”, the tiny channels which are impermeable for ordinary liquids.

To solidify  $^4\text{He}$ , a minimum pressure of about 25 bars is required. At these pressures the most common lattice structure of helium crystals is hexagonal close packed (*hcp*), besides that there exists only a tiny region where the lattice is a body centered cubic (*bcc*), see Fig. 2. At very high pressures (above 1000 bar), the  $^4\text{He}$  lattice can be face centered cubic (*fcc*). Most of the experimental studies on  $^4\text{He}$  crystals have been performed for the *hcp* phase, including the measurements presented in this Thesis.

The melting curve of  $^4\text{He}$  nearly flattens below 0.9 K, where the entropies of the solid

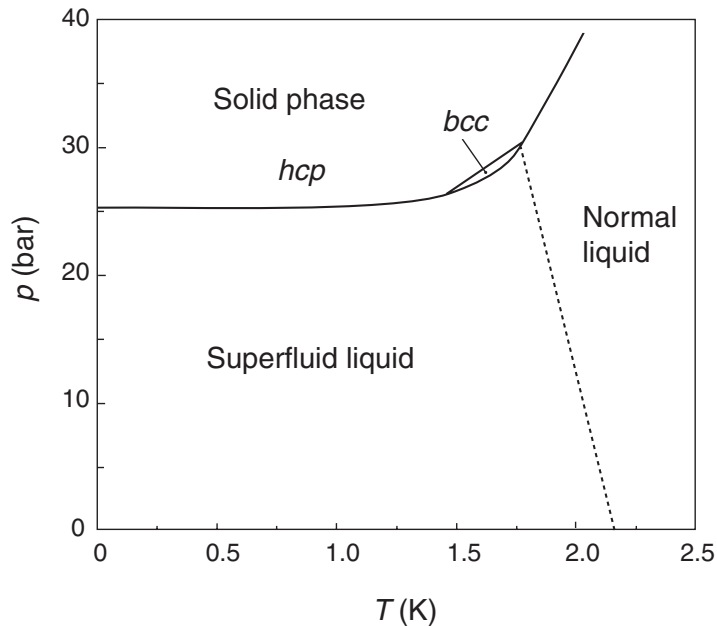


Figure 2: Liquid-solid phase diagram of  $^4\text{He}$ .

and liquid phases are very small. In this temperature range, growth dynamics becomes fast and the  $^4\text{He}$  crystals can follow the pressure deviations from equilibrium in a time scale of milliseconds. Under such unique conditions it becomes possible to observe weakly damped melting-freezing waves on the rough crystal surface [4, 7]. As a consequence,  $^4\text{He}$  crystals are able to reach their equilibrium shape almost instantly.

Optical measurements on  $hcp$ - $^4\text{He}$  crystals have revealed three different roughening transitions. The first facet observed was the **c**-facet (0001), the basal plane of the hexagonally symmetric  $^4\text{He}$  with the highest roughening temperature,  $T_{R1} = 1.3$  K [8, 9, 14]. When lowering the temperature, six **a**-facets ( $1\bar{1}00$ ) appear on the vertical edge of the crystal at  $T_{R2} = 0.9$  K [8, 14]. Below  $T_{R3} = 0.36$  K, **s**-facets ( $1\bar{1}01$ ) are formed between the **c**- and **a**-facets [15]. This evolution of the equilibrium shape of a helium crystal as a function of temperature is illustrated in Fig. 3.

As mentioned above, according to Ref. [1], crystals are expected to become completely faceted as temperature is decreased. However, no new roughening transitions have been observed in  $^4\text{He}$  down to 2 mK [13].

The rough and faceted crystal surfaces grow differently. Owing to thermal and quantum fluctuations, a certain density of nucleation sites is always present on the rough surfaces, so these surfaces have no threshold for their growth. Facets grow slowly because there is a problem in finding a landing site for an atom to stick to.

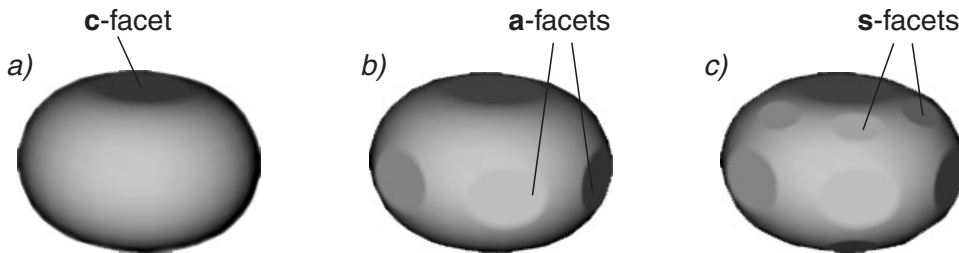


Figure 3: Shape of  $^4\text{He}$  crystals at different temperatures. For simplicity, the effect of gravity is neglected. a) The presence of **c**-facets at  $T_{R1} < 1.28$  K. b) Appearance of the six **a**-facets at  $T_{R2} < 0.9$  K. c) The  $^4\text{He}$  crystal shape with all observed facets; **c**, **a** and **s**-facets at  $T_{R3} < 0.35$  K.

The growth kinetics of  $^4\text{He}$  crystals has been studied in detail on rough surfaces [16], on facets [13] and on surfaces in the vicinity of the facet edge [17]. This Thesis presents results on how even very small amounts of  $^3\text{He}$  atoms can influence the spiral growth of **c**-facets, which is governed by screw dislocations. The measurements reveal the reduction of growth velocities with the increase of  $^3\text{He}$  concentration, and yield an estimation of the effective width of an elementary step on the interface [P7].

## 1.2 $^3\text{He}$ crystals

Compared with  $^4\text{He}$ ,  $^3\text{He}$  is a very rare (and expensive!) element. It is mainly obtained as a byproduct in industrial nuclear reactors. The phase diagram of  $^3\text{He}$  in Fig. 4 is more complicated than that of  $^4\text{He}$ . The  $^3\text{He}$  gas liquefies at a temperature of 3.2 K ( $p = 1$  bar).

A  $^3\text{He}$  atom has a nuclear spin of  $1/2$  and a collection of  $^3\text{He}$  atoms obeys Fermi-Dirac quantum statistics. Similar to  $^4\text{He}$ , it also becomes superfluid, but at a much lower temperature ( $T_C = 2.5$  mK at melting pressure). However, the underlying physics here is completely different and the pairing of  $^3\text{He}$  atoms can be described in terms of the BCS theory [18]. The complicated broken-symmetry state characterizing the superfluidity leads to the existence of several distinct superfluid phases, or different pairing states. In zero magnetic field, the *A*-phase is stable only in a small region of temperature and pressure near  $T_C$  while the main body of the phase diagram is occupied by the *B*-phase.

The light mass of a  $^3\text{He}$  atom and the correspondingly large zero-point energy require a pressure of about 34 bar to solidify liquid  $^3\text{He}$  at  $T = 0$  K. Up to 100 bar,  $^3\text{He}$  crystals possess the *bcc*-lattice structure. At higher pressures the *hcp* and *fcc* structures can form as well. Optical studies of  $^3\text{He}$  crystals were conducted only for the *bcc*-phase.

The phase diagram of  $^3\text{He}$  crystals has a low-temperature side of the melting curve

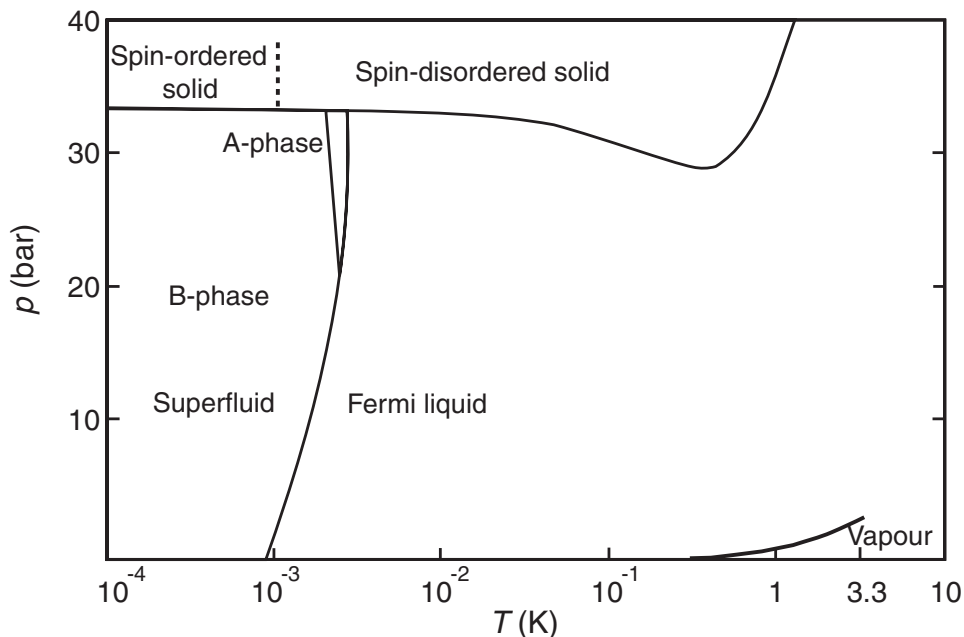


Figure 4: Phase diagram of  $^3\text{He}$ .

with a negative slope, which is due to the lower entropy of the liquid in comparison with that of the solid phase. The entropy of the solid is that of a system of disordered nuclear spins and is equal to  $R \ln 2$ , until the spins order at the Néel temperature,  $T_N = 0.93$  mK. The entropy of liquid  $^3\text{He}$ , which behaves as a Fermi liquid below 1 K, decreases linearly with temperature well below its Fermi temperature. At the minimum of the melting curve ( $p_{\min} = 29.315$  bar,  $T_{\min} = 319$  mK) [19] the entropies of liquid and of solid are equal. Such unusual behavior in solid  $^3\text{He}$  was predicted by Pomeranchuk [20].

As temperature deviates from that of the melting curve minimum, the large latent heat along with the poor thermal conductivity of liquid  $^3\text{He}$  results in very slow shape-relaxation times. Well below the ordering transition in the solid phase, the latent heat of crystallization decreases rapidly, the surrounding liquid is in the superfluid state, and  $^3\text{He}$  crystals are expected to show fast growth kinetics similar to  $^4\text{He}$  crystals [4].

Solid  $^3\text{He}$  can be studied by nuclear magnetic resonance (NMR) due to its intrinsic spin angular momentum of  $\hbar/2$ . Ultralow temperature ( $T < 1$  mK) NMR measurements of single  $^3\text{He}$  crystals were pioneered by Osheroff *et al.* [21]. The first growth-rate measurements were performed by Feng *et al.* [22]. NMR studies on the melting of  $^3\text{He}$  crystals reported that below  $0.78 T_N$  the melting rate was too rapid to be measured quantitatively [23]. The much slower growth velocities were attributed to the presence of slowly growing facets which have screw dislocations. Unfortunately, the NMR measurements

provide only indirect information on the surface state and direct visualization is required.

The equilibrium shape of  $^3\text{He}$  crystals has been observed only in the vicinity of the melting curve minimum where the latent heat of crystallization is very low [24]. At this temperature the crystals are nicely rounded and facets are not present.

The first facets of (110) type on the surface of growing  $^3\text{He}$  crystals have been detected at  $T \lesssim 100$  mK [25]. The measured roughening transition temperature  $T_{\text{R1}} = 100$  mK, however, should be taken with caution since in this temperature region the shapes of the  $^3\text{He}$  crystals are highly sensitive to the growth conditions.

Two more types of facets, (100) and (211), have been identified in  $^3\text{He}$  during crystal growth from the superfluid phase at  $T \geq 0.7$  mK [26, 27]. The highest temperature where these facets were observed has been reported to be about 10 mK. The crystal growth rates, measured at  $T = 0.7$  mK [27], showed good agreement with the earlier NMR measurements. However, only the average growth velocity of the crystal has been reported. In these experiments, the crystal images were analyzed using two-dimensional projections of facet edges.

In our measurements, *bcc*- $^3\text{He}$  crystals were imaged with a low-temperature multiple-beam interferometer [P1, P2]. Altogether, eleven types of facets were identified on the crystal surface at a temperature of 0.55 mK [P3–P6] and the growth rates were measured for almost all of the observed facets [P5].

## 2 Experimental apparatus

### 2.1 Ultralow temperature probe for optical measurements on $^3\text{He}$ crystals

All measurements described in this Thesis were performed with help of the “Interface” low-temperature facility of the Low Temperature Laboratory at Helsinki University of Technology. This cryostat has been modified to conduct optical studies of helium interfaces at low temperatures. The first cooling stage of the cryostat is a commercial dilution refrigerator, Oxford 600 [28]. The original mixing chamber of the refrigerator has been replaced with a custom-made one that has an effective heat-exchange area of  $600\text{ m}^2$ . In performance tests, the modified cryocooler reached a base temperature of  $5.0\text{ mK}$ . It was also possible to achieve a cooling power of  $5.3\text{ }\mu\text{W}$  at  $15\text{ mK}$  with a circulation rate of  $500\text{ }\mu\text{mole/s}$ . A melting-curve thermometer and a nuclear-orientation thermometer were used to monitor the temperature of the cryostat during the performance tests.

Several different interferometric schemes were utilized in the measurements, the actual geometry of each was determined by the goals of the particular experiment. However, all optical schemes shared a common principle: all vital optical components, with the exception of a He-Ne laser and a shutter, were located inside the 4-K vacuum jacket of the cryostat.

To study the morphology and growth kinetics of  $^3\text{He}$  crystals well below  $1\text{ mK}$  the experimental setup used previously [13] was considerably remodeled. A sketch of the latest optical arrangement is depicted in Fig. 5. The optics was completely redesigned: the incoming and outgoing optical arms are now more separated, which simplifies the optical design and adjustments. Most of the optical components (the beam expander, the beam splitter and the light dumper) are housed below the mixing chamber to minimize the optical path length between the end of the fiber and the interferometer. They are thermally anchored to the cold plate ( $T \approx 70\text{ mK}$ ) in order to reduce the heat load to the mixing chamber of the dilution refrigerator.

The heart of our optical system is a Fabry-Pérot multiple-beam interferometer with a phase-shift feature [P1–P3]. The multiple-beam interferometry allows us to observe the whole crystal shape as well as the fine details on the solid/liquid interface. It also enables us to significantly reduce the imaging light intensity, which is very essential at ultralow temperatures. As compared with the two-beam path interferometry principle, the multiple-beam interferometry allows a simpler experimental implementation and sharper

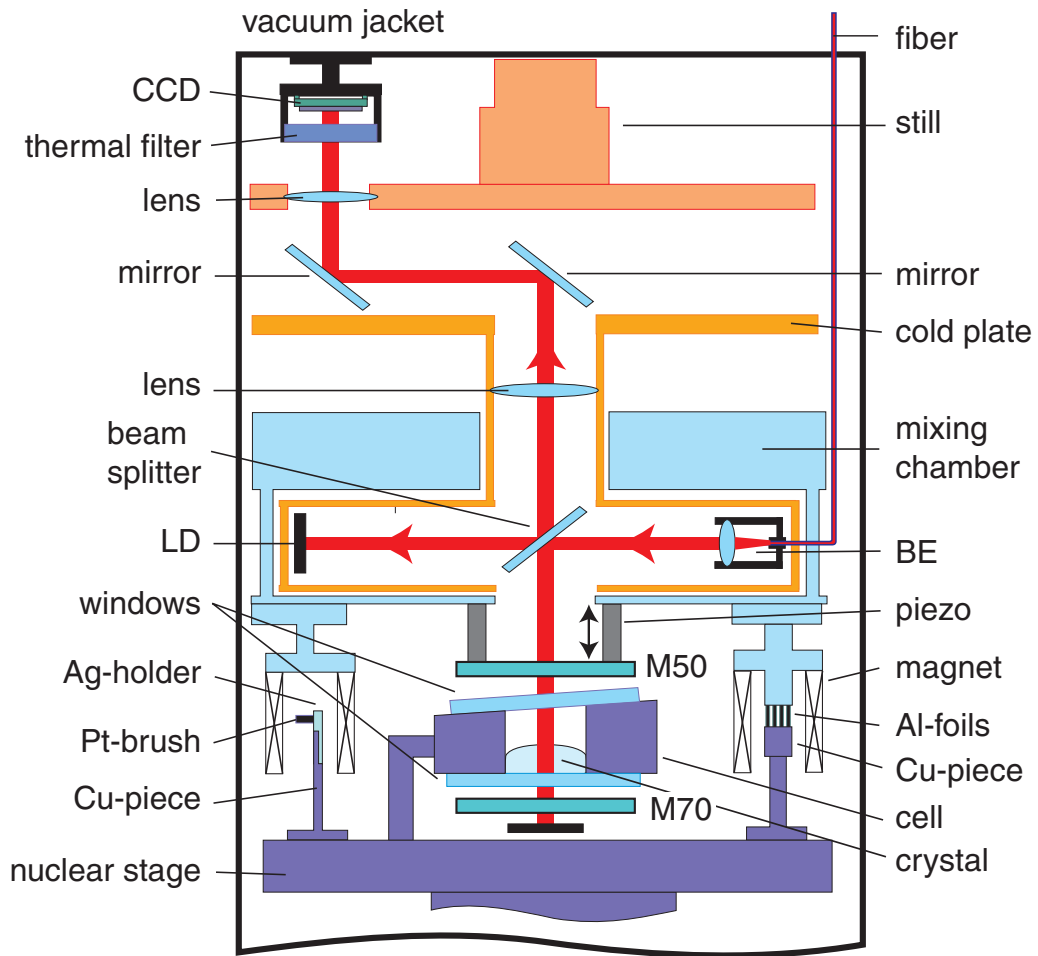


Figure 5: Layout of the setup for  $^3\text{He}$  crystal studies: Charge Coupled Device (CCD), light dumpers (LD), beam expander (BE), M50 and M70 - mirrors with 50% and 70% reflectivity. For details, see text.

fringes.

The optical part of the cell has a cylindrical copper body ( $\varnothing = 16$  mm,  $h = 12$  mm), which is sealed off by two fused-silica windows with an antireflection coating on all the optical surfaces. A multiple-beam interferometer is formed by two parallel mirrors with 50% (M50) and 70% (M70) reflectivities, placed above and below the cell. Both mirrors are thermally anchored to the mixing chamber of the dilution refrigerator. The top mirror can be moved in the vertical direction by a cylindrical piezoelectric crystal to which this mirror is attached.

A He-Ne laser beam ( $\lambda = 632.8$  nm) is guided into a single-mode fiber that enters the vacuum jacket, where the beam expander (BE) widens it to a diameter of 8 mm. Via a 50% beam splitter the beam enters the interferometer through the top mirror (M50). The light

undergoes multiple reflections between the mirrors and the interference pattern, formed by the interfering beams, is reflected back through the top mirror. An objective and a periscope focuses it to a cooled slow scan CCD-sensor which has  $575 \times 383$  light-sensitive elements (pixels). A thermal filter (8 mm of  $\text{CaF}_2$ ) cuts off the thermal radiation from the CCD-sensor (operated at about 80 K) from entering the cell. The “unused” beams are absorbed by light dumpers (LD) made of black velvet.

The vertical resolution in the interface position achieved in this instrument is a few micrometers, while the horizontal resolution of about  $15 \mu\text{m}$  is limited by the pixel size of the CCD-imager. Crystal surfaces with a slope less than  $70^\circ$  with respect to the bottom mirror of the interferometer could be resolved.

A new nuclear demagnetization stage of the cryostat was designed and constructed as well. The new stage has 104 moles of copper in total, while the effective amount of 36.6 moles is in a magnetic field of 8 T. Before installation, the copper stage was carefully annealed in a vacuum oven at  $960^\circ\text{C}$  for 100 h. The nuclear stage is fixed to the mixing chamber of the dilution refrigerator by four rods made of  $\text{SiO}_2$ . The adjustable thermal link between the mixing chamber and the nuclear stage is achieved with a superconducting heat switch made of four aluminium foils. The aluminium foils were connected to the copper pieces by diffusion bonding. The total electrical resistance of the heat switch measured at 4.2 K was  $44 \text{ n}\Omega$ .

To monitor the temperature of the nuclear stage, a new platinum NMR thermometer was built. The platinum sensor is a brush of 1100 high-purity  $25 \mu\text{m}$  Pt-wires, arc-welded to a silver holder. The Pt-thermometer was calibrated at low temperatures 6 to 25 mK against the primary  $^{60}\text{Co}$  nuclear orientation thermometer.

As mentioned above, the melting curve of  $^3\text{He}$  has a minimum at  $T = 319 \text{ mK}$ , see Fig. 4. If temperature is lowered below the minimum, it becomes impossible to change the liquid pressure in the cell from room temperature: the filling line will always have a plug of solid  $^3\text{He}$ . The standard solution to this problem is to use a Pomeranchuk-type cell [20].

Figure 6 illustrates the practical design used to build our experimental cell. The total inner volume of the cell is about  $13 \text{ cm}^3$  and it can be changed up to 8% by means of BeCu bellows. The cross-section area of the  $^4\text{He}$  bellows is roughly three times larger than that of the  $^3\text{He}$ -side, thus the  $^4\text{He}$  pressure must be kept in the range 6 to 10 bars. Calibrated flows of  $^4\text{He}$  were used to compress the cell to grow the  $^3\text{He}$  crystals.

The optical part has a ring made of Stycast 1266 [29] with a diameter of 18 mm, see

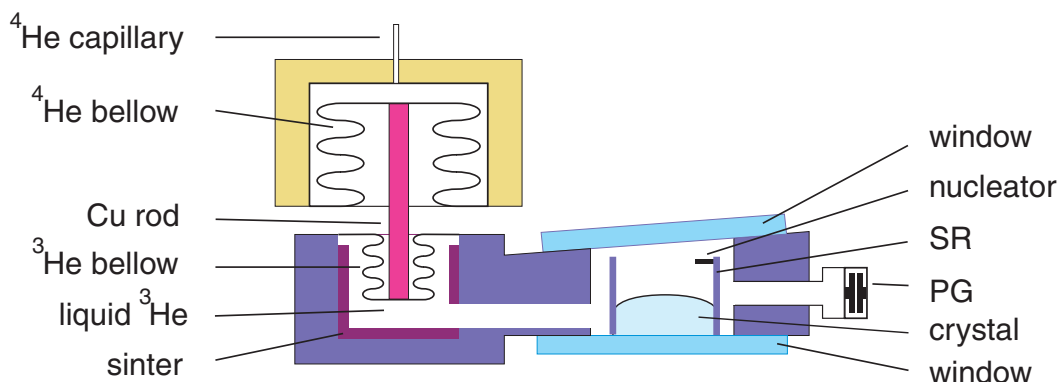


Figure 6: Experimental  $^3\text{He}$  cell. Pressure gauge (PG) and Stycast ring (SR). For details, see text.

Fig. 6. It stops the direct flow of the liquid to the optical part of the cell while pressurizing and also serves as a holder for the tungsten-tip nucleator, to which a high voltage can be applied. The nucleator is placed just outside the field of view to ensure that crystals will appear at the desired spot in the cell.

The  $^3\text{He}$  pressure was monitored with capacitance measurements using a Straty-Adams type strain gauge [30] implemented in the cell. The BeCu membrane of the gauge is 0.4 mm thick and has a diameter of 9 mm. On each cooldown from room temperature, the pressure gauge was calibrated at 1 K. The resolution of the pressure gauge is a few  $\mu\text{bar}$  at 35 bars, when measured with an AH 2500A capacitance bridge [31]. The pressure of  $^4\text{He}$  was monitored at room temperature.

The experimental cell is thermally connected to the copper nuclear stage and liquid  $^3\text{He}$  is cooled via a silver heat exchanger having an effective area of 50 to 60  $\text{m}^2$ . The temperature in the cell was determined from the equilibrium melting curve pressure using Adams' temperature scale [32]. The temperature calibration was checked after every demagnetization: the small  $^3\text{He}$  crystal was kept in the cell during warmup [P5].

## 2.2 Setup for c-facet studies on $^4\text{He}$ crystals

Figure 7 illustrates the scheme of the optical setup for  $^4\text{He}$  crystal studies. It is quite similar to the one described in the preceding Section. The goal of the experiments was to study the growth of the **c**-facet in the presence of small amounts of  $^3\text{He}$  atoms. The desired temperature range was above 20 mK and we removed the nuclear demagnetization stage and concomitant devices.

The crystals were grown inside an optical experimental chamber monitored by a two-



capacitive nucleator–bifilar coil wound around a bakelite holder, placed outside the field of view.

The liquid and solid phases of  $^4\text{He}$  have approximately a 0.7% difference in their dielectric permittivity. This was employed to measure the position and the growth velocity of the liquid/solid interface. The level gauge (interdigital capacitor) was mounted on the cell wall and it has a vertically aligned fingered structure (finger width  $10\ \mu\text{m}$ , spacing  $10\ \mu\text{m}$ ), produced by evaporating a thin layer of chromium on fused-silica glass.

The liquid pressure in the cell was monitored with a Straty–Adams type strain gauge [30]. The thickness and the diameter of the gauge membrane are 0.3 mm and 9 mm, respectively. The resolution of the gauge is about  $0.3\ \mu\text{bar}$  at 25 bars, when measured with a high-precision AH 2500A capacitance bridge [31]. The pressure gauge was calibrated against the hydrostatic pressure change encountered during crystal growth through the whole 4.8 mm range of the level gauge. The temperature was measured with a carbon resistor, calibrated against the melting-curve and nuclear-orientation thermometers.

## 3 Experiments on solid-liquid interface of $^3\text{He}$

### 3.1 Nucleation of crystals

It is commonly known that it is extremely difficult to nucleate and grow single  $^3\text{He}$  crystals from the normal liquid. The negative latent heat of crystallization, which is absorbed during the growth of the crystal, cools down the surrounding liquid. Since the thermal conductivity of the normal liquid is rather poor, the temperature gradients in the experimental cell are large. As a result, it becomes favorable to nucleate a new crystal seed somewhere else in a warmer spot instead of growing the already present crystal. Figure 8a shows several  $^3\text{He}$  crystals which were nucleated in the field of view from the normal liquid.

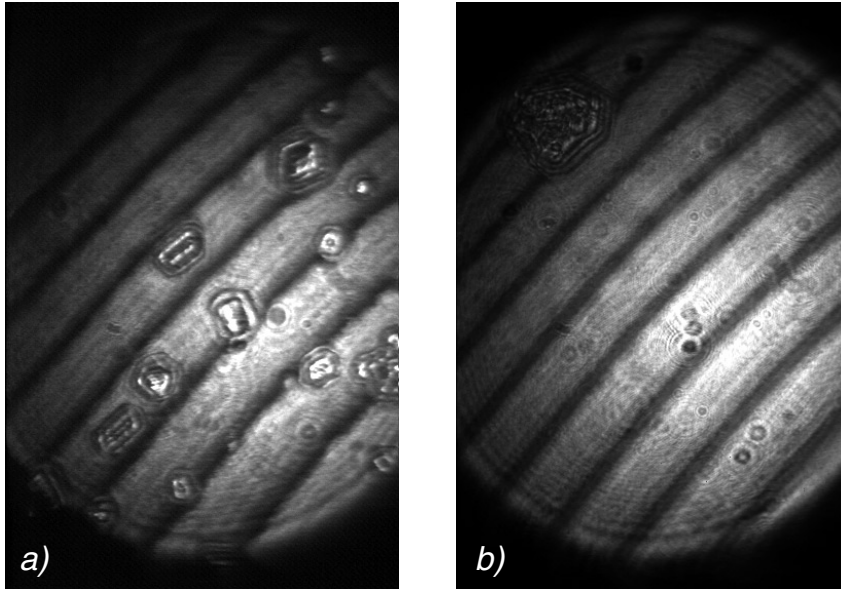


Figure 8: a) Multiple crystals nucleated from normal liquid  $^3\text{He}$ . b) A single  $^3\text{He}$  crystal nucleated at  $T = 0.78$  mK with  $-900$  V applied to the nucleator. The background pattern arises from the liquid helium wedge (due to the  $2^\circ$ -tilt of the top window) and non-parallel alignment of the mirrors.

Single crystals of  $^3\text{He}$  can be produced relatively easily below  $T_N = 0.93$  mK where the latent heat of crystallization is significantly reduced and the surrounding liquid is superfluid. After the liquid  $^3\text{He}$  was cooled to the desired temperature, the nucleation of the solid phase from the superfluid  $^3\text{He}$  was obtained by increasing the pressure of  $^3\text{He}$  above the melting curve. Figure 9 presents the pressure trace of one of the nucleation

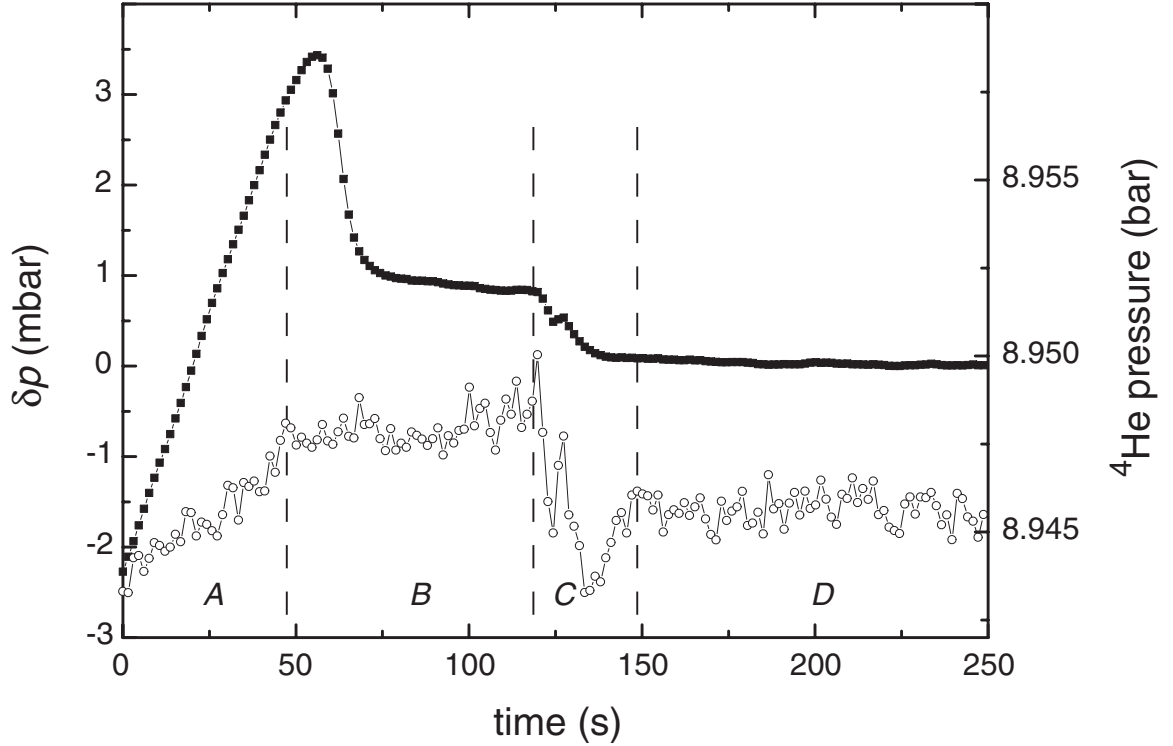


Figure 9: Pressure trace during  $^3\text{He}$  crystal nucleation, measured at  $T = 0.78$  mK, displaying (■)  $^3\text{He}$  pressure variation from the melting curve value and (o)  $^4\text{He}$  pressure.

events at  $T = 0.78$  mK. This crystal, see Fig. 8b, was created with a high voltage ( $-900$  V) applied to the nucleator.

In the beginning of the experiment, compression of the  $^3\text{He}$ -cell was started with a constant mass flow of  $^4\text{He}$  from the room-temperature ballast volume. The  $^4\text{He}$ -flow was kept constant until region *C* where the cell compression was stopped. Region *A* corresponds to the all-liquid state, an increase of the  $^3\text{He}$  and  $^4\text{He}$  pressures is induced by a flow of  $^4\text{He}$ . The change of slope of the  $^4\text{He}$  pressure during the constant compression rate (region *B*) is due to a nucleation of solid  $^3\text{He}$  and the subsequent supply of matter required for its growth. Shortly after the appearance of the crystal, it grows rather fast and reduces the excess pressure  $\delta p$  to a constant level, which is determined by the mechanism of crystal growth, the cell compression rate and temperature. After the  $^4\text{He}$ -flow was stopped (*C*) the pressure relaxes towards the equilibrium melting curve value  $\delta p = 0$  (region *D*). For nucleation and for crystal growth,  $\delta p$  is 2.6 and 0.90 mbar, respectively.

Attempts to nucleate crystals in the field of view with pulses of laser light having

different duration (up to 2 min) were not successful. The application of a high voltage (up to  $-900$  V) to the nucleator in order to enhance the pressure locally by high electric field did produce a crystal seed in the field of view at a few times lower excess pressure than that for the spontaneous nucleation.

## 3.2 Morphological studies

The equilibrium crystal shape reflects the internal structure of the crystal lattice along with other properties. For example, crystals with a repulsive step-step interaction can exhibit the “devil’s staircase” — the presence of facets with arbitrarily high Miller indices ( $hkl$ ) on the crystal surface [34–36]. This phenomenon has been recently observed in lyotropic liquid crystals where the crystal surface revealed almost 60 different types of facets [37]. The planes which are most likely to appear as external facets are the ones with the highest reticular density which is directly proportional to the interplanar spacing  $d_{hkl}$  for a given type of plane [38]. In the *bcc*-lattice  $d_{hkl} = a/2(h^2 + k^2 + l^2)^{1/2}$ , where  $a$  is the lattice constant.

The number of facets expected to be present at a given temperature can be estimated from:

$$k_B T_R = \frac{2}{\pi} \sqrt{\gamma_{\parallel} \gamma_{\perp}} d^2, \quad (1)$$

where  $k_B$  is the Boltzmann constant,  $T_R$  the roughening transition temperature of a particular facet,  $d$  the interplanar distance (height of an elementary step on the facet) and  $\gamma_{\parallel}$  and  $\gamma_{\perp}$  the principal components of the surface stiffness for that surface [1, 2]. Both components of  $\gamma$  should be measured at a temperature above — but close to — the expected transition temperature for that part of the surface.

In any crystal the angles between the different types of facets have fixed values. This property was used to identify each of the observed facets on the  $^3\text{He}$  crystal surface. The measured angles between the facets were compared with the theoretically possible ones for the ideal *bcc*-structure. Of course, one can find a large number of facets which are infinitesimally close to each other and that satisfy the selection criteria within experimental precision. However, we have always chosen the most “stable” facets consistent with the experimentally determined angles.

Analysis of the crystal morphology was usually started from samples which had the lowest number of facets and then proceeded to the more complicated ones. First, each facet (region with equidistant parallel fringes on the interferogram) was selected and the corresponding normals were found. Then a conversion to the physical sizes was carried

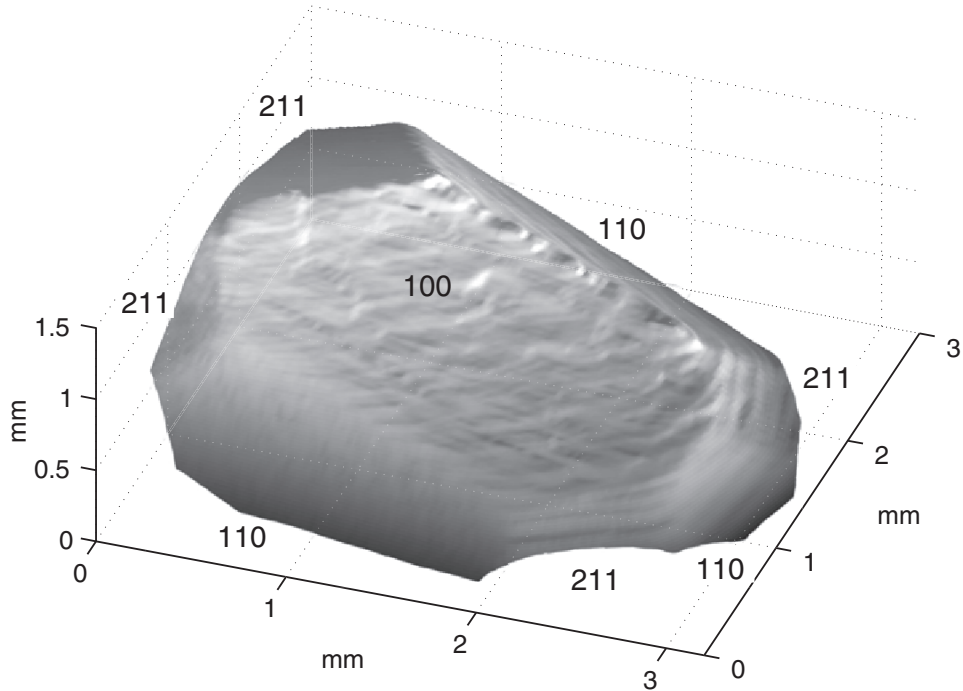


Figure 10: Surface profile of a  $bcc\text{-}^3\text{He}$  crystal measured at  $T = 0.55$  mK. Three types of facets, (110), (110) and (211), are present.

out, and the angles between the different regions were calculated. Next a guess for the facet type was made and, subsequently, the angles between all facets were cross-checked.

Two different approaches were utilized to determine the normals of the facets on the observed crystals. A phase-shift technique [39], which yields a simple and reliable measurement of the surface profile of the crystal was applied when a crystal was under stable conditions. Intensity-based analysis methods [40], which require only single interferograms, were used during the crystal growth. Both methods yielded the same results and are described in detail elsewhere [P3, P5]. Figure 10 illustrates an example of the surface profile of a  $^3\text{He}$  crystal measured with the phase-shift technique.

During the measurements, altogether eleven types of facets were observed on the surface of  $bcc\text{-}^3\text{He}$  crystals at  $T = 0.55$  mK. Figure 11 indicates the positions of these facets on one elementary patch of the whole crystal habit. Also the positions of those facets which were not observed, but have a higher (or equal) reticular density and thus a higher (or equal) roughening temperature than the (311) plane, are shown in Fig. 11 as open circles.

Each of the facets identified was detected on more than one interferogram and at least

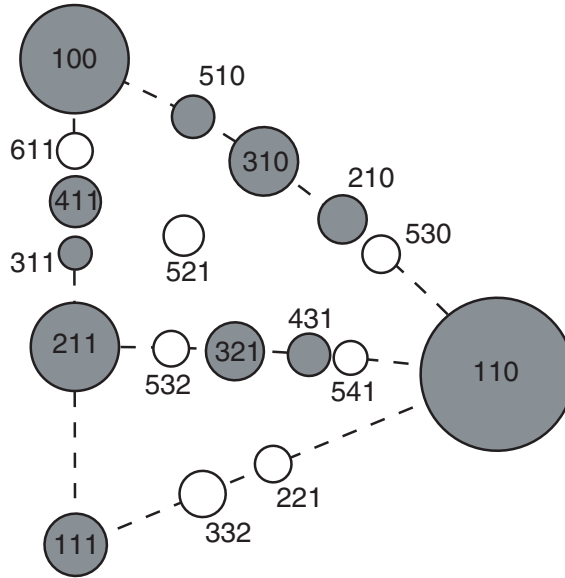


Figure 11: Diagram with the Miller indices of facets in the *bcc* structure of  $^3\text{He}$ . Filled points represent experimentally observed facets, empty ones correspond to facets expected to be seen. The diameters of the circles are proportional to the interplanar distance. The coordinates are obtained by projecting to the  $[111]$  plane the points at which the corresponding facet normals pass through the surface of a spherical crystal.

three equally spaced parallel fringes were observed. The typical difference between the expected and measured angles was up to  $2^\circ$ ; in the worst cases it was around  $6^\circ$  for the shortest fringes. All facets were uniquely determined with the exception of the (510) facet which is rather close to the (410) facet, but as mentioned above in such cases the most “stable” facets were chosen.

### 3.3 Anisotropy of growth kinetics

Most of the facets identified were visible at a non-zero growth rate. Crystals were grown and melted at constant temperature by compressing or decompressing the cell with a controlled flow of  $^4\text{He}$  from the ballast volume at room temperature. During growth, images of the crystals were taken every 4 s.

Most of the growth measurements were started with rounded crystals. Almost immediately after the growth was initiated, the facets appeared and the crystals became completely faceted. The sizes of the facets appeared to be mainly determined by the shape of the crystal just before growth.

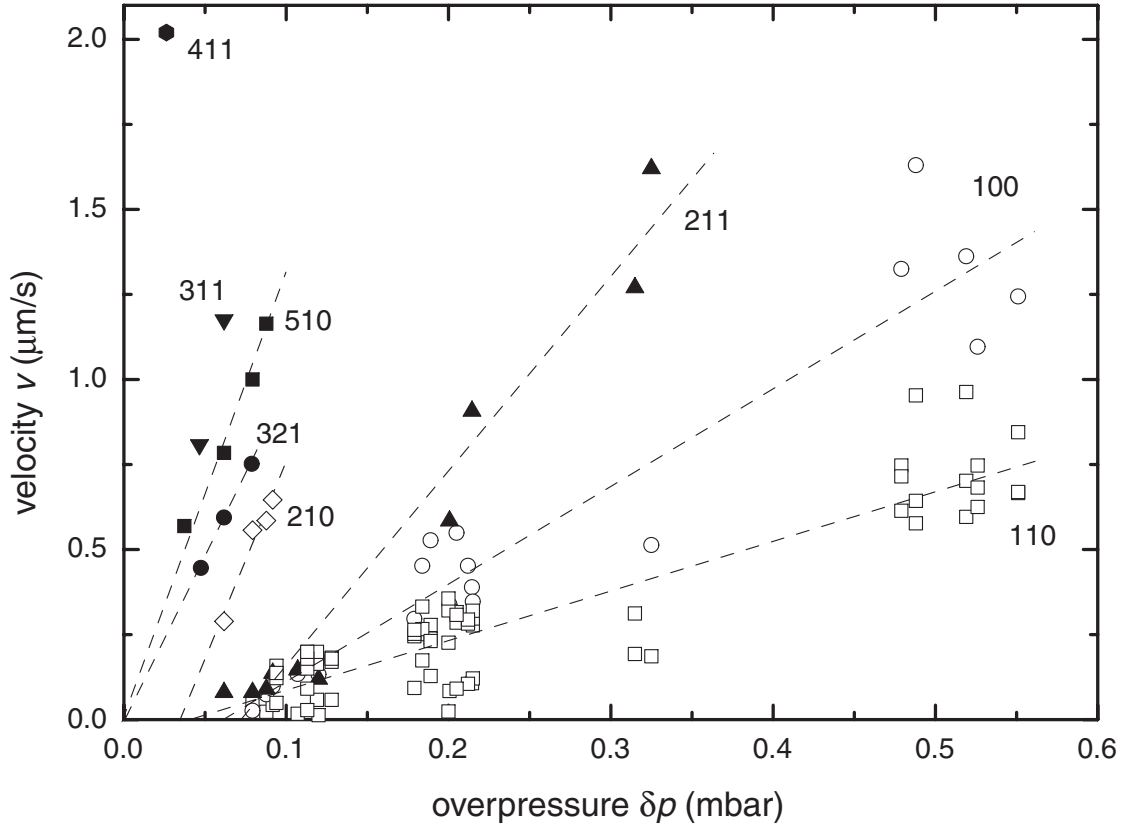


Figure 12: Anisotropy of  $^3\text{He}$  crystal growth at  $T = 0.55$  mK.

The analysis pointed out that, initially, mostly facets with high Miller indices covered the crystal surface. When the growth was continued, the slowly growing densely populated facets increasingly determined the shape of the crystal. Typically, only the two most “stable” facets, (110) and (100), remained on the final crystal shape. When the growth was stopped the facets diminished and the crystal became more rounded on a time scale of some tens of seconds.

The growth rates were measured for most of the observed facets. The growth velocities were calculated by tracking the positions of fringes between the subsequent interferograms [P5]. Figure 12 summarizes the growth rates obtained for the different types of facets. The scatter in the growth velocities and overpressure values are not determined by the resolution of the measurement technique, but rather have a physical origin. The higher the applied overpressure was, the larger were the deviations, and during melting of the crystal the scatter in pressure was approximately ten times smaller.

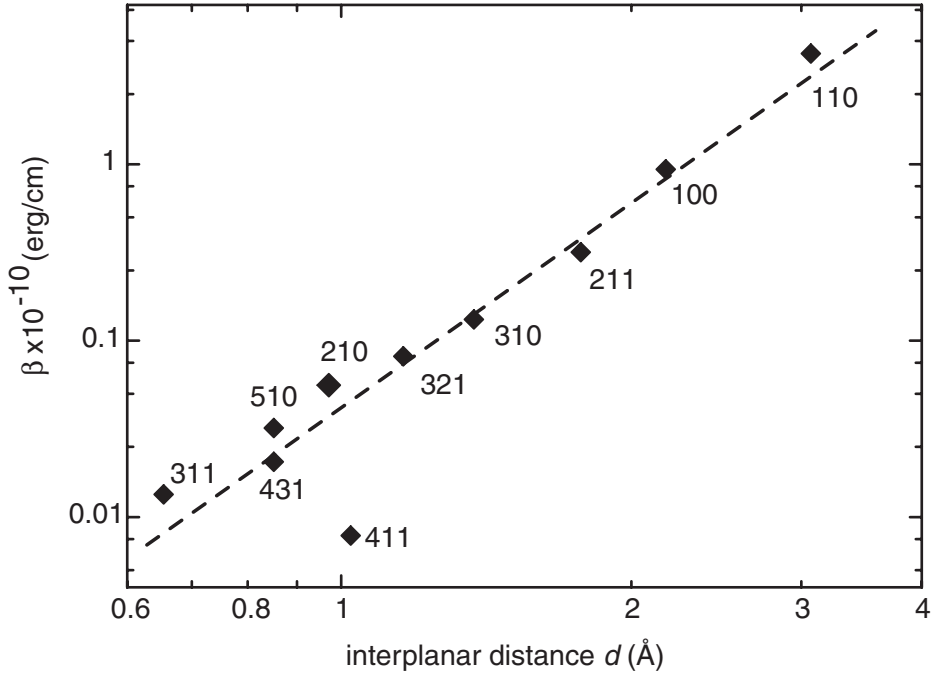


Figure 13: Step energies of different facets on a  $^3\text{He}$  crystal at  $T = 0.55$  mK. The linear fit has a slope of  $3.9 \pm 0.5$ .

The observed growth displays rather strong anisotropy: for instance, the velocities of the (110) and (510) facets differ by about one order of magnitude. The nearly linear dependence of the growth velocity on the applied driving force suggests that the dominating growth mechanism is spiral growth in the regime of suppressed step mobility [13,41]. The growth rate of a smooth surface when the step speed exceeds critical velocity  $v_c$  is [P5]:

$$v = \frac{v_c d^2}{2\pi\beta} \frac{\Delta\rho}{\rho_l} K \delta p. \quad (2)$$

Here  $d$  and  $\beta$  are the height and free energy of an elementary step,  $\Delta\rho$  is the difference between the densities of the solid ( $\rho_s$ ) and liquid ( $\rho_l$ ) phases,  $\delta p$  is the difference between the actual pressure and the equilibrium melting curve value and  $K$  is the number of steps produced by one dislocation. The lowest critical velocities in  $^3\text{He}$  are the magnon velocity  $c$  and the pair-breaking velocity  $v_{\text{pb}}$ . At low magnetic fields both are approximately equal to 7-8 cm/sec [42,43].

The step energies of different facet types were calculated from the measured growth velocities using Eq. (2). In the calculations it was assumed that one dislocation produces a single step [P5]. The step energies obtained are plotted in Fig. 13. The linear fit in

Table 1: Miller indices of the experimentally observed types of facets, their reciprocal lattice vectors  $\langle hkl \rangle$ , the squared interplanar distance ratio with respect to the (110) facet, the measured free energy of the elementary step  $\beta$ , and the highest temperature  $T_{\text{obs}}^{\text{max}}$  at which the facet has been observed.

Miller index	$\langle h k l \rangle$	$(d_{110}/d_{hkl})^2$	$\beta$ (erg/cm)	$T_{\text{obs}}^{\text{max}}$ (mK)
110	$\langle \frac{1}{2} \frac{1}{2} 0 \rangle$	1	$4.2 \cdot 10^{-10}$	100 [25]
100	$\langle 1 0 0 \rangle$	2	$9.5 \cdot 10^{-11}$	10 [26]
211	$\langle 1 \frac{1}{2} \frac{1}{2} \rangle$	3	$3.2 \cdot 10^{-11}$	$<10$ [26]
310	$\langle 1 \frac{1}{2} \frac{1}{2} 0 \rangle$	5	$1.3 \cdot 10^{-11}$	0.55
111	$\langle 1 1 1 \rangle$	6	—	0.55
321	$\langle 1 \frac{1}{2} 1 \frac{1}{2} \rangle$	7	$8.1 \cdot 10^{-12}$	0.55
411	$\langle 2 \frac{1}{2} \frac{1}{2} \rangle$	9	$8 \cdot 10^{-13}$	0.55
210	$\langle 2 1 0 \rangle$	10	$5.6 \cdot 10^{-12}$	0.55
510	$\langle 2 \frac{1}{2} \frac{1}{2} 0 \rangle$	13	$3.2 \cdot 10^{-12}$	0.55
431	$\langle 2 1 \frac{1}{2} \frac{1}{2} \rangle$	13	$2.1 \cdot 10^{-12}$	0.55
311	$\langle 3 1 1 \rangle$	22	$1.3 \cdot 10^{-12}$	0.55

the log-log coordinates yields approximately a quartic power-law dependence of the free energy on the height of an elementary step.

The theoretical calculations conducted by Landau in the case of van der Waals interaction between elementary steps ( $r^{-3}$ ) reported on the fifth power dependence of the free step energy versus the height of the step [44]. Similar calculations for the step-step interactions of elastic origin ( $r^{-2}$ ) resulted in fourth power dependence [45], thus measurements conducted agree well with later model.

Table 1 lists all the identified types of facets with the corresponding step free energies obtained. The energy  $\beta_{110}$  of an elementary step on the (110) facet is equal to  $4.2 \cdot 10^{-10}$  erg/cm. Unexpectedly this value is the same as that observed in  $^4\text{He}$  crystals for the (1000) facet [17]. According to Nozières [2], at any temperature below  $T_{\text{R}}$  the width of an elementary step  $\xi$  is connected to the free energy of the step as follows:

$$\xi\beta \sim k_{\text{B}}T_{\text{R}}. \quad (3)$$

The calculated width of the elementary step  $\xi_{110}$  equals 2-3 lattice constants, which is one quarter of that in  $^4\text{He}$ . As mentioned above, the step width reflects the strength of coupling between the interface and crystal lattice. In  $^4\text{He}$ , the step width of approximately

10  $a$  has been attributed to the rather weak coupling [2, 17]. The smaller step width in  $^3\text{He}$  crystals suggests that the coupling of the interface to the crystal lattice is stronger.

The measurements of the melting velocity seem to be a far more difficult task than that of growth. The underpressure developed is small, the crystal is changing its curvature, and the velocity is rather high. The analysis showed that crystals initially melt very fast near the edges between facets, and the melting rate slows down as the crystals achieve a certain shape or a larger surface is involved in the melting.

At a temperature of 0.55 mK, the average melting velocity  $v$  was  $1.67 \mu\text{m/s}$  with the corresponding overpressure  $\delta p = -11.3 \mu\text{bar}$  [P5]. These measurements yield the effective growth coefficient

$$k_{\text{eff}} = \frac{\rho_s \rho_l}{(\Delta\rho)} \frac{v}{\delta p} = 2.3 \cdot 10^{-3} \text{ s/m}. \quad (4)$$

The growth rate of a rough surface, which should be essentially the same as that for melting, was also measured [P5]. During 8 s the crystal gained about  $60 \mu\text{m}$  in height, while the overpressure was about  $65 \mu\text{bar}$ . The volume of the crystal grown is in good agreement with the cell-compression rate, which was  $5.3 \cdot 10^{-5} \text{ cc/s}$  of solid  $^3\text{He}$ . The calculated effective growth coefficient  $k_{\text{eff}} = 2.6 \cdot 10^{-3} \text{ s/m}$  is close to the value obtained during melting.

The growth and melting velocities of rough surfaces were about two times higher than the growth rate of the fastest facet (411). Thus processes measured on smooth surfaces exhibit intrinsic properties and are not limited by thermal impedances of the bulk phases as in the case of rough surfaces.

During melting some of the most “stable” facets were preserved, which suggests that they should be observed on the equilibrium crystal shape. The equilibrium size of any facet  $L_{\text{hkl}}$  is proportional to the free energy of the step [44]:

$$L_{\text{hkl}} \approx \beta_{\text{hkl}} R / (d_{\text{hkl}} \gamma), \quad (5)$$

where  $R$  is a characteristic size of the crystal and  $\gamma$  is the surface stiffness. Using  $\gamma = \gamma_0 = 0.06 \text{ erg/cm}$ , measured at high temperatures [25], and the step energies obtained, it is easy to estimate the equilibrium sizes of the facets. The equilibrium size of the (110) facet should be approximately  $0.2R$  and the higher-order facets should be smaller. The typical size of the crystals studied was 4-10 mm, which means that the (110) facets should be easily detected with optical observations.

Unfortunately, the equilibrium sizes of the facets were not measured. The observed crystals were either growing or melting due to the pressure instabilities in the  $^4\text{He}$  filling

line caused by the thermal effects. In order to measure the equilibrium shape of the crystal, a low-temperature valve should be installed in the system.

## 4 Growth kinetics of c-facets of $^4\text{He}$ crystals

Spiral growth of  $hcp$ - $^4\text{He}$  crystals was studied with 40 ppm, 110 ppm and 220 ppm of  $^3\text{He}$  atoms in the liquid phase in the temperature range of  $10 \text{ mK} \leq T \leq 225 \text{ mK}$ . Initially, a crystal was nucleated at  $T \approx 20 \text{ mK}$  from regular commercial helium, with nominal  $^3\text{He}$  concentration less than 100 ppb. Two-beam interferometry was employed to obtain a crystal with its **c**-facet almost parallel to the reference plate.

The number of  $^3\text{He}$  atoms was gradually increased each time after the complete series of growth measurements were accomplished with the current concentration. The mixture was prepared using calibrated ballast volumes at room temperature and a new concentration of  $^3\text{He}$  in the cell was achieved by driving helium in and out of the cell. Prior to adding the  $^3\text{He}$ , the crystal was always melted to a small size, since the amount of  $^3\text{He}$  atoms dissolved in the solid phase is negligible for temperatures well below 0.3 K [46].

While the crystal was periodically grown and melted, the level of the solid-liquid interface and the liquid pressure were simultaneously monitored. The measured growth velocities [P7] were described with the classical spiral growth (quadratic) dependence [2, 13]

$$v = \frac{\Lambda\mu}{\pi\beta} \left( \frac{\Delta\rho}{\rho} \right)^2 a^2 \delta p^2. \quad (6)$$

Here  $\beta/a = 0.011 \text{ erg/cm}^2$  [17] is the free energy of a step,  $a$  is the lattice constant,  $\Lambda = 0.33095\dots$  is a constant, and  $\delta p$  is the pressure deviation from the equilibrium melting curve value.

The step mobility  $\mu$  is determined by the friction due to the step colliding with phonons and with  $^3\text{He}$  atoms in the bulk liquid. The collisions of the steps with phonons dominate at temperatures  $T \geq 100 \text{ mK}$  and the corresponding growth resistance (inverse mobility) is  $1/\mu_{\text{ph}} \propto T^3$  [17]. Since at  $T < 100 \text{ mK}$  the phonon resistance is very small, the scattering of impurities plays a major role.

For the range of temperatures ( $T \geq 10 \text{ mK}$ ) and low concentrations, the  $^3\text{He}$  atoms in the liquid behave as a nondegenerate 3D Fermi gas [47]. The contribution of the impurities to the growth resistance due to elastic scattering at the interface is predicted to be equal to

$$\frac{1}{\mu_{\text{sc}}} = \frac{\sqrt{2} a^2 \sqrt{m_3 T}}{\pi \xi} n_3, \quad (7)$$

where  $\xi$  is the effective step width,  $m_3$  and  $n_3$  are the effective mass and the concentration of  $^3\text{He}$  atoms in the liquid, respectively. The total growth resistance including both mechanisms is the sum,  $1/\mu = 1/\mu_{\text{sc}} + 1/\mu_{\text{ph}}$ .

Figure 14 presents the step mobilities obtained as a function of temperature for different  $^3\text{He}$  concentrations. As the concentration of  $^3\text{He}$  atoms is increased, there is a clear decrease in the mobilities at low temperatures, in accordance with the theory presented in Ref. [47]. The solid lines were calculated by fitting the  $^3\text{He}$  collision mobilities to the data, and summing the respective contributions to the growth resistance. The phonon-limited mobility was fitted to the high-temperature data as  $1/\mu_{\text{ph}} = AT^3$ , where  $A$  is a fit parameter, yielding  $A = 10^{-7.5} \text{ g/s cm K}^3$ . The effective step width  $\xi$  was estimated by fitting Eq. (7) to the mobility data at temperatures  $T \leq 100 \text{ mK}$ , resulting in  $\xi = 5 \pm 2 \text{ nm}$ .

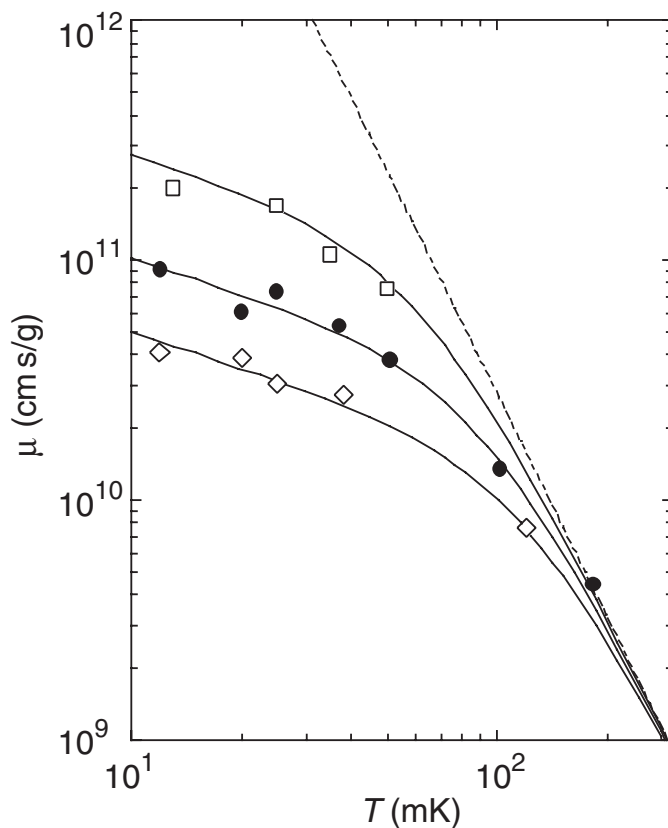


Figure 14: Step mobilities  $\mu$  calculated from measurements with  $^3\text{He}$  concentrations of 40 ppm ( $\square$ ), 110 ppm ( $\bullet$ ), and 220 ppm ( $\diamond$ ). Earlier data, measured with regular  $^4\text{He}$  (purity 0.1 ppm) by Ruutu *et al.* [13] are represented by the dashed line. The solid lines denote theoretical curves, calculated using an effective step width of  $\xi = 5 \text{ nm}$  (see text for details).

This value is larger than the one currently assumed in the “weak-coupling” picture [17, 48], and it also exceeds the estimate  $\xi \approx 3 \text{ nm}$  obtained from zero-point oscillations [47]. When discussing the difference between the calculated and measured values of  $\xi$ , one

should recall that the calculations were made using the simple harmonic approximation which is not expected to be very accurate in the case of such large amplitudes. From this point of view, the measured value of  $\xi$  rather than the calculated one should be considered as a new and important characteristic of the step structure.

## 5 Discussion

This Thesis reports on studies of solid-liquid helium interfaces at ultralow temperatures. All research was conducted in the Interface group in the Low Temperature Laboratory at Helsinki University of Technology.

A new low-temperature setup was designed and constructed for interferometric studies of both of the stable helium isotopes. Multiple-beam interferometry was employed for investigations of the morphology and growth kinetics of  $^3\text{He}$  crystals below 1 mK. The experimental setup with a two-beam interferometer was used for growth studies of the *c*-facet in  $^4\text{He}$  crystals.

The  $^3\text{He}$  crystals were nucleated and grown at a lowest temperature of  $T = 0.55$  mK. The growth measurements revealed altogether eleven types of facets as compared with only three facets observed previously. The number of facets obtained is in good agreement with theory, which predicts an even larger amount of the facets at this temperature. All types of facets were identified within the framework of a simple *bcc*-lattice, and possible effects of the antiferromagnetic (*u2d2*) structure were not considered.

The growth rates of the rough and smooth surface states were explored. Both the growth and melting of the rough crystal surface yielded for the effective growth coefficient a value of 2 to  $3 \cdot 10^{-3}$  s/m, which is influenced by the thermal impedances of the bulk phases at a temperature of 0.55 mK.

The growth velocities of facets were slower than those of rough surfaces and they revealed a significant anisotropy. The growth rates of different facets varied by more than an order of magnitude. The measurements conducted exhibit a linear dependence of the facet velocity on the overpressure applied, which points out that the main growth mechanism is spiral growth in the regime of suppressed mobility.

The calculated step energies of the facets in  $^3\text{He}$  crystals feature a quartic dependence on the step height and suggest that the steps experience elastic interactions. The step energy of the most “stable” (110) facet is equal to  $4.2 \cdot 10^{-10}$  erg/cm and the corresponding step width ( $\xi_{110} \sim 2$  to  $3 a$ ) reflects relatively strong coupling of the interface to the crystal lattice.

The sizes of the equilibrium facets estimated from the free energy of the step show that the most “stable” facets, (110) and (100), should be observed on the crystal surface, while the higher-order facets, such as (311) or (411), can be more easily detected during crystal growth. Unfortunately, the equilibrium facet sizes were not studied in the present measurements.

A low-temperature valve for the  $^4\text{He}$  filling capillary is strongly recommended for future measurements on equilibrium crystal shapes. Studies of the actual roughening transition temperatures are necessary to prove the validity of current theories. The growth measurements of rough surfaces at lower temperatures and their temperature dependence should reveal the feasibility of melting-freezing waves in  $^3\text{He}$ . The optical measurements with magnetic fields can provide information on the crystal shape influenced by the magnetic structure of the lattice.

The measurements of the spiral growth on the  $\mathbf{c}$ -facet in  $^4\text{He}$  crystals were conducted in the presence of small amounts of  $^3\text{He}$  in liquid  $^4\text{He}$  in the temperature range of  $10 \text{ mK} < T < 225 \text{ mK}$ . In the phonon collision regime ( $T > 100 \text{ mK}$ ), good agreement was found with earlier measurements by Ruutu *et al.* [13]. The decrease of the growth velocities at low temperatures was attributed to the elastic scattering off the moving step of the nondegenerate 3D Fermi gas. The analysis of the growth rates for different amounts of impurities resulted in the step width of  $5 \pm 2 \text{ nm}$ . The obtained value is in reasonable agreement with theoretical predictions and shows rather “weak” coupling between the interface and crystal lattice in  $^4\text{He}$ .

The measurements on the interface mobility conducted with both isotopes result in a rather large step width in  $^4\text{He}$  and a smaller one in  $^3\text{He}$ . This result is somehow surprising since  $^3\text{He}$  has larger zero-point fluctuations. However, maybe it is due to the influence of the magnetic structure which is present in the  $^3\text{He}$  crystals. Another question which is raised by the measurements conducted: why have only three types of facets been observed in  $^4\text{He}$  crystals? Is it a property of the *hcp*-structure, the very high mobility of the interface, or just lack of careful measurements? It would be interesting to measure the shape of  $^4\text{He}$  crystals using the new setup which has been developed. However, a real-time high-resolution imaging sensor is probably required due to the high mobility of the interface.

## 6 Publications

This Thesis is based on the following original publications:

**P1.** J. P. H. Härme, H. Alles, A. Babkin, R. Jochemsen, A. Ya. Parshin, V. Tsepelin, and G. Tvalashvili, *Optical Observations of  $^3\text{He}$  Crystals at mK-Temperatures*, *Physica B* **284-288**, 349 (2000).

The new optical setup is described, which employs multiple-beam interferometry for measurements on  $^3\text{He}$  crystals. The first images of  $^3\text{He}$  crystals obtained with a phase-shift technique are presented.

**P2.** V. Tsepelin, H. Alles, A. Babkin, J. P. H. Härme, R. Jochemsen, A. Ya. Parshin, and G. Tvalashvili, *Nucleation and Growth of  $^3\text{He}$  Crystals below 1 mK*, *Physica B* **284-288**, 351 (2000).

The first measurements on the nucleation of  $^3\text{He}$  crystals at temperatures down to 0.55 mK are described. The growth kinetics of the solid-liquid interface was studied by combining a low-temperature multiple-beam interferometer and high-precision pressure measurements. Preliminary results on the effective growth coefficient are presented.

**P3.** V. Tsepelin, H. Alles, A. Babkin, J. P. H. Härme, R. Jochemsen, A. Ya. Parshin, and G. Tvalashvili, *Direct Observation of (110), (100) and (211) Facets on  $^3\text{He}$  Crystals*, *J. Low Temp. Phys.* **121**, 695 (2000).

A systematic description of the phase-shift technique and its application to  $^3\text{He}$  crystal-morphology studies is presented. Optical observations on  $^3\text{He}$  crystals grown from the superfluid phase below 1 mK are reported. The angles between the crystal facets were measured and the surface profiles of the observed crystals were reconstructed on the basis of the information obtained. Three different types of facets, (110), (100) and (211), were clearly visible in these experiments.

**P4.** V. Tsepelin, H. Alles, A. Babkin, J. P. H. Härme, R. Jochemsen, A. Ya. Parshin, and G. Tvalashvili, *Observation of Higher Order Facets on  $^3\text{He}$  Crystals*, *Phys. Rev. Lett.* **86**, 1042 (2001).

Faceting was observed on  $^3\text{He}$  crystals investigated with a low-temperature Fabry-

Pérot interferometer. Altogether nine types of facets were identified during the growth of a  $bcc$ - $^3\text{He}$  single crystal at a temperature of 0.55 mK. The number of facets observed under our experimental conditions was compared with dynamic roughening theory.

**P5.** V. Tsepelin, H. Alles, A. Babkin, R. Jochemsen, A. Ya. Parshin, I. Todoshchenko, and G. Tvalashvili, *Morphology and Growth Kinetics of  $^3\text{He}$  Crystals below 1 mK*, TKK report (2001).

Growth and melting of  $^3\text{He}$  crystals investigated with a low temperature Fabry-Pérot interferometer are reported. Eight new types of facets were observed during growth of  $bcc$ - $^3\text{He}$  single crystals at temperature well below 1 mK. The interferogram analysis based on intensity methods is described in detail. The growth-rate anisotropy for faceted crystals was measured and a linear dependence of the growth velocity on the driving force was observed. The free energies of the steps were calculated and results obtained suggest that coupling of the solid-liquid interface to the lattice in  $^3\text{He}$  is stronger than was expected.

**P6.** H. Alles, V. Tsepelin, A. Babkin, R. Jochemsen, A. Ya. Parshin and I. Todoshchenko, *Observations on Faceting of  $^3\text{He}$  Crystals at  $T = 0.55$  mK*, accepted for publication in *J. Low Temp. Phys.* (2001).

Recent observations, in which on growing  $^3\text{He}$  crystals in total eleven different types of facets were found, are described. The facets were identified with the phase-shift technique and intensity-based analysis methods. The possible reasons why only three types of facets have been observed in  $^4\text{He}$  crystals are discussed.

**P7.** V. Tsepelin, J. P. Saramäki, A. V. Babkin, P. J. Hakonen, J. J. Hyvönen, R. M. Luusalo, A. Ya. Parshin, and G. K. Tvalashvili, *Elementary Steps on the  $^4\text{He}$  Crystal Interface Probed by  $^3\text{He}$  Atoms*, *Phys. Rev. Lett.* **83**, 4804 (1999).

The growth dynamics of **c**-facets, studied in the temperature range of  $10 < T < 225$  mK in the presence of low concentrations of  $^3\text{He}$  atoms in the liquid, is described. The interactions of  $^3\text{He}$  atoms with moving elementary steps induced by the screw dislocations are considered. The results are in a good agreement with the theory, where high-frequency zero-point oscillations of the steps are taken into account, if an effective step width  $\xi \approx 5$  nm is assumed.

## 7 The author's contribution

The research work presented in this Thesis is a result of team work.

Starting from March 1996 as a group member, I was involved in all phases of the design, construction and testing of the new experimental setup for  $^3\text{He}$  crystal studies. I had major responsibility of the day-to-day operations and maintenance of the cryostat from the beginning of 1997 to early 2000.

All of the measurements presented (for  $^3\text{He}$  and  $^4\text{He}$ ) were carried out by myself. I wrote the main part of the software for the measurements and data analysis. I have also conducted most of the data analysis of the  $^3\text{He}$  crystal measurements. I was involved in the initial stages of the  $^4\text{He}$  data analysis.

I was mainly responsible for the writing of publications P2–P5.

## Acknowledgements

I wish to express my gratitude to Prof. Mikko Paalanen, the Director of the Low Temperature Laboratory, for supervision during my work.

I would like to thank Prof. Pertti Hakonen for originally giving me the chance to work in the Low Temperature Laboratory. I am especially grateful to my supervisor Prof. Alex Babkin and my colleague Dr. Giorgi Tvalashvili for their guidance and expertise during my first years in the Interface group. I want to thank the present group leader Dr. Harry Alles for his enthusiasm and trust. I am deeply indebted to Acad. Alexander Parshin for providing excellent theoretical support. I wish to acknowledge Dr. Reyer Jochemsen for his advice on experiments and help with writing papers. I owe much to Dr. Sergei Boldarev for teaching me skills necessary to work with dilution refrigerators. I am obliged to my other co-workers in the Interface-group: Anke Husmann, Jörkki Hyvönen, Juho Härme, Jussi Ruutu, Jari Saramäki, Reeta Tarkiainen, and Igor Todoshchenko. I also wish to thank all visitors who have participated in the work of the Interface-group: Acad. Konstantin Keshishev, Mitja Kholin, Evgeny Nazaretski, and Alex Majorov.

I enjoyed the long hours in the laboratory and outside with my colleagues, Rob Blaauwgeers, Tauno Knuuttila, Juha Kopu, Juha Martikainen, and Jaakko Ruohio.

I have benefited from discussions with A. Andreev, P. Berglund, V. Eltsov, N. Kopnin, M. Krusius, K. Nummila, Ü. Parts, J. Penttilä, L. Roschier, R. Schanen, E. Thuneberg, and G. Volovik. I am grateful to Prof. Martti Salomaa for his valuable comments on the manuscript. I also wish to thank my pre-examiners Prof. Emil Polturak and Prof. Martti Puska for reviewing the manuscript.

I would like to thank T. Halme, M. Holmström, P. Kinanen, T. Koivisto, S. Pakarinen, and L. Pasanen for their help with practical matters. I owe much to A. Huvila, A. Isomäki, and A. Salminen for the reliable delivery of liquid helium. Special thanks to the skillful machinists of the workshop J. Kaasinen, S. Kaivola, H. Kaukelin, M. Korhonen, S. Lehtovuori, and K. Rauhala.

The whole staff of the Low Temperature Laboratory is thanked for a friendly and inspiring atmosphere.

I would like to thank my wife Irina for her patience and encouragement. Finally, I thank my parents and other relatives for their support during all these years. Last but not least I express my gratitude to all my friends, who made my life in Finland fun.

Viktor Tsepelin

## References

- [1] D. S. Fisher and J. D. Weeks, Phys. Rev. Lett. **50**, 1077 (1983).
- [2] P. Nozières, in *Solids Far From Equilibrium*, ed. C. Godrèche (Cambridge University Press, Cambridge, 1991).
- [3] C. Rottman and M. Wortis, Phys. Reports **103**, 59 (1984), and references therein.
- [4] A. F. Andreev and A. Ya. Parshin, Zh. Eksp. Teor. Fiz. **75**, 1511 (1978) [Sov. Phys. JETP **48**, 763 (1978)].
- [5] A. Ya. Parshin, in *Low Temperature Physics*, ed. A. S. Borovik-Romanov (MIR Publishers, Moscow, 1985).
- [6] S. Balibar and B. Castaing, Surf. Sci. Rep. **5**, 87 (1985); S. Balibar and P. Nozières, Solid State Comm. **92**, 19 (1994).
- [7] K. O. Keshishev, A. Ya. Parshin, and A. V. Babkin, Pis'ma Zh. Eksp. Teor. Fiz. **30**, 63 (1979) [JETP Lett. **30**, 56 (1979)].
- [8] J. E. Avron, L. S. Balfour, C. G. Kuper, J. Landau, S. G. Lipson, and L. S. Schulman, Phys. Rev. Lett. **45**, 814 (1980).
- [9] S. Balibar and B. Castaing, J. Physique Lett. **41**, L-329 (1980).
- [10] A. J. Manninen, J. P. Pekola, G. M. Kira, J. P. Ruutu, A. V. Babkin, H. Alles, and O. V. Lounasmaa, Phys. Rev. Lett. **69**, 2392 (1992).
- [11] R. Wagner, P. J. Ras, P. Remeijer, S. C. Steel, and G. Frossati, J. Low Temp. Phys. **95**, 715 (1994).
- [12] H. Alles, J. P. Ruutu, A. V. Babkin, P. J. Hakonen, A. J. Manninen, and J. P. Pekola, Rev. Sci. Instrum. **65**, 1784 (1994).
- [13] J. P. Ruutu, P. J. Hakonen, A. V. Babkin, A. Ya. Parshin, and G. Tvalashvili, J. Low Temp. Phys. **112**, 117 (1998).
- [14] K. O. Keshishev, A. Ya. Parshin, and A. V. Babkin, Zh. Eksp. Teor. Fiz. **80**, 716 (1981) [Sov. Phys. JETP **53**, 362 (1981)].
- [15] P. E. Wolf, S. Balibar, and F. Gallet, Phys. Rev. Lett. **51**, 1366 (1983).
- [16] C. L. Wang and G. Agnolet, Phys. Rev. Lett. **69**, 2102 (1992).
- [17] E. Rolley, E. Chevalier, C. Guthmann, and S. Balibar, J. Low Temp. Phys. **99**, 851 (1995).
- [18] J. Bardeen, L. N. Cooper, and J. R. Schrieffer, Phys. Rev. **108**, 1175 (1957).
- [19] E. R. Grilly, J. Low Temp. Phys. **4**, 615 (1971).

- [20] I. Pomeranchuk, Zh. Eksp. Teor. Fiz. **20**, 919 (1950).
- [21] D. D. Osheroff, M. C. Cross, and D. S. Fisher, Phys. Rev. Lett. **44**, 792 (1980).
- [22] Y. P. Feng, *NMR studies of the  $u2d2$  nuclear antiferromagnetic phase of bcc solid helium three* (Ph.D. Thesis, Stanford University, 1991).
- [23] R. Nomura, H. H. Hensley, T. Matsushita, and T. Mizusaki, J. Low Temp. Phys. **94**, 377 (1994).
- [24] F. Graner, S. Balibar, and E. Rolley, J. Low Temp. Phys. **75**, 69 (1989).
- [25] E. Rolley, S. Balibar, F. Gallet, F. Graner, and C. Guthmann, Europhys. Lett. **8**, 523 (1989).
- [26] R. Wagner, S. C. Steel, O. A. Andreeva, R. Jochemsen, and G. Frossati, Phys. Rev. Lett. **76**, 263 (1996); R. Wagner, *The observation of  $^3\text{He}$  crystals at temperatures down to 1 mK using a cooled CCD camera* (Ph.D. Thesis, Leiden University, 1995).
- [27] H. Akimoto, R. v. Rooijen, A. Marchenkov, R. Jochemsen, and G. Frossati, Physica **B 255**, 19 (1998).
- [28] Manufactured by Oxford Instruments, Oxfordshire, OX8 1TL, UK.
- [29] Stycast 1266 (transparent), manufactured by Emerson and Cummings, Canton, Massachusetts, 02021, USA.
- [30] G. C. Straty and E. D. Adams, Rev. Sci. Instr. **40**, 1393 (1969).
- [31] Andeen-Hagerling 2500A, Andeen-Hagerling, Inc., 31200 Bainbridge Rd., Cleveland, Ohio 44139-2231, USA.
- [32] W. Ni, J. S. Xia, E. D. Adams, P. S. Haskins, and J. E. McKisson, J. Low Temp. Phys. **101**, 305 (1995).
- [33] P. J. Hakonen, H. Alles, A. V. Babkin, and J. P. Ruutu, J. Low Temp. Phys. **101**, 41 (1995) and references therein.
- [34] C. Herring, Phys. Review **82**, 87 (1951).
- [35] H. J. Schulz, J. Physique **46**, 257 (1985).
- [36] S. E. Burkov, J. Physique **46**, 317 (1985).
- [37] P. Pieranski, P. Sotta, D. Rohe, and M. Imperor-Clerc, Phys. Rev. Lett. **84**, 2409 (2000).
- [38] F. C. Philips, *An Introduction to Crystallography* (Longmans, New York, 1960).
- [39] G. Bönsch and H. Böhme, Optik **82**, 161 (1989).
- [40] D. W. Robinson and G. T. Reid, *Interferogram Analysis* (IOP Publishing Ltd., 1993).

- [41] A. A. Chernov, *Modern Crystallography III: Crystal Growth* (Springer-Verlag, 1984).
- [42] D. D. Osheroff and C. Yu, *Phys. Lett.* **77**, 458 (1980).
- [43] Y. P. Feng, P. Shiffer, D. D. Osheroff and M. C. Cross, *J. Low Temp. Phys.* **90**, 475 (1993).
- [44] L. D. Landau, *Collected Papers* (Pergamon Press, Oxford, 1971).
- [45] V. I. Marchenko and A. Ya. Parshin, *JETP* **52**, 129 (1980).
- [46] See, *e.g.*, D. O. Edwards and S. Balibar, *Phys. Rev. B* **39**, 4083 (1989), and references therein.
- [47] A. Ya. Parshin, *J. Low Temp. Phys.* **110**, 133 (1998).
- [48] M. Uwaha and P. Nozières, *J. Physique (Paris)* **48**, 407 (1987).